Nb-Mediated Grain Growth and Grain-Boundary Engineering in Mg_3Sb_2-Based Thermoelectric Materials

Ting Luo, Jimmy J. Kuo, Kent J. Griffith, Kazuki Imasato, Oana Cojocaru-Mirédin, Matthias Wuttig, Baptiste Gault, Yuan Yu,* and G. Jeffrey Snyder*

The poor carrier mobility of polycrystalline Mg_3Sb_2 at low temperatures strongly degrades the thermoelectric performance. Ionized impurities are initially thought to dominate charge carrier scattering at low temperatures. Accordingly, the increased electrical conductivity by replacing Mg with metals such as Nb is also attributed to reduced ionized impurity scattering. Recent experimental and theoretical studies challenge this view and favor the grain boundary (GB) scattering mechanism. A reduction of GB scattering improves the low-temperature performance of $Mg_3(Sb, Bi)_2$ alloys. However, it is still elusive how these metal additions reduce the GB resistivity. In this study, Nb-free and Nb-added Mg_3Sb_2 are studied through diffraction, X-ray absorption spectroscopy, solid-state nuclear magnetic resonance spectroscopy, and atom probe tomography. It is shown that Nb does not enter the Mg_3Sb_2 matrix and remains in the metallic state. Besides, Nb diffuses along the GB forming a wetting layer, which modifies the interfacial energy and accelerates grain growth. The GB resistivity appears to be reduced by Nb-enrichment, as evidenced by modeling the electrical transport properties. This study not only confirms the GB scattering in Mg_3Sb_2 but also reveals the hitherto hidden role of metallic additives on enhancing grain growth and reducing the GB resistivity.

1. Introduction

n-type Mg_3Sb_2 has attracted ever-increasing attention in recent years due to its outstanding thermoelectric performance in the low- to intermediate-temperature range.[1] It is thus a promising alternative to commercial Bi_2Te_3-based alloys that are more expensive and mechanically unstable.[1g,2] For a long period only p-type Mg_3Sb_2 was obtained due to p-type intrinsic defects, for example, Mg vacancies.[3] The figure-of-merit zT of p-type Mg_3Sb_2 is lower than its n-type counterpart, in part due to the lack of energy band complexity.[4] Owing to the pioneering work of Tamaki et al.,[1b] and Iversen et al.,[4] a high zT of above 1.5 was obtained in n-type polycrystalline $Mg_3Sb_{1.5}Bi_{0.5}$-based compounds with excess Mg and various dopants.[5] This finding ignited extensive research interest in n-type Mg_3Sb_2 in recent years.[3b,6]

As reported by Tamaki et al.,[1b] polycrystalline $Mg_{3.2}Sb_{1.5}Bi_{0.49}Te_{0.01}$ exhibits reduced carrier mobility with decreasing temperature below 500 K, which largely degrades the electrical conductivity and low-temperature thermoelectric performance. The reduced carrier mobility was first attributed to ionized impurity scattering, but it was later shown to be a grain boundary (GB) effect.[1b,7] A reduction of GB scattering makes $Mg_3(Sb, Bi)_2$ alloys competitive to commercial Bi_2Te_3.[1e,8] Simply increasing the grain size without changing the composition can improve the low-temperature carrier mobility and zT.[9] Kuo et al.[7b] proposed a model based upon a GB phase with a band offset compared to the grain interior phase, and this model shows good agreement with measured grain size dependencies of electrical conductivity. The chemical nature of the GB phase was further revealed by atom probe tomography (APT),[10] which indicated that the Mg deficiency at GBs is responsible for the high GB resistivity.[10a] Compensation of this deficiency via Mg-vapor annealing along with increased grain size can improve low-temperature zT.[8a] Single-crystal electrical transport property measurements have further proven the absence of ionized impurity scattering in Mg_3Sb_2.[8b,11]

Nevertheless, there have been several reports that the low-temperature carrier mobility can be improved by the addition of various metals at the expense of added Mg, such as Mn,[1c,12] Co,[12b,13] (Fe, Hf, Ta),[13] and Nb.[7a] This improvement of carrier mobility was attributed to the reduction of ionized

Dr. T. Luo, Dr. B. Gault
Max-Planck-Institut für Eisenforschung GmbH
Max-Planck-Straße 1 40237, Düsseldorf, Germany

Dr. J. J. Kuo, Dr. K. J. Griffith, Dr. K. Imasato, Prof. G. J. Snyder
Department of Materials Science and Engineering
Northwestern University
Evanston, IL 60208, USA
E-mail: jeff.snyder@northwestern.edu

Dr. O. Cojocaru-Mirédin, Prof. M. Wuttig, Dr. Y. Yu
Institute of Physics IA
RWTH Aachen University
52056 Aachen, Germany
E-mail: yu@physik.rwth-aachen.de

Prof. M. Wuttig
PGI 10 (Green IT)
Forschungszentrum Jülich GmbH
52428 Jülich, Germany

Dr. B. Gault
Department of Materials
Royal School of Mines
Imperial College
Prince Consort Road, London SW7 2BP, UK

impurity scattering with the assumption that metal elements substitute the Mg sites. For example, Shuai et al. reported that the carrier mobility of $Mg_{3.2}Sb_{1.5}Bi_{0.49}Te_{0.01}$ was improved from 19 cm^2 V^{-1} s^{-1} to 77 cm^2 V^{-1} s^{-1} at room temperature by adding 10% Nb at the expense of Mg.[7a] If the high resistivity of Mg_3Sb_2-based alloys at low temperatures is due to GB scattering rather than ionized impurity scattering, the role of Nb to enhance the low-temperature mobility is indicative of a previously unexplored phenomenon. It could thus possibly lead to new strategies to improve thermoelectric properties.

In this work, two samples with nominal compositions of $Mg_{3.05}Sb_{1.99}Te_{0.01}$ and $Nb_{0.1}Mg_{3.05}Sb_{1.99}Te_{0.01}$ were investigated to understand the mechanisms underpinning the high performance in Nb-added Mg_3Sb_2; denoted here as Mg_3Sb_2 and $Nb_{0.1}$-Mg_3Sb_2, respectively. The effect of additive Nb on the thermoelectric properties of Mg_3Sb_2 was studied by comprehensive structural and chemical characterization techniques. We show that Nb appears to be wetting the GB, speeding up grain growth, rather than entering the Mg_3Sb_2 matrix. This new evidence supports the idea that the improved electrical conductivity of $Nb_{0.1}$-Mg_3Sb_2 is not due to weakened ionized impurity scattering but as a result of reduced GB resistivity. A similar mechanism is expected in other metal-added n-type Mg_3Sb_2 alloys.[1c,7a,12,13] We call it metal-added rather than doped because these metals do not enter the matrix as will be evidenced in this work. The present work demonstrates that advanced thermoelectric materials could be developed through GB engineering, including but not limited to Mg_3Sb_2–Mg_3Bi_2 alloys, for example, $Mg_3Sb_{1.5}Bi_{0.5}$, half-Heusler alloys, and $SrTiO_3$.

2. Elemental Nb Probed by XRD, NMR, and XAS

X-ray diffraction (XRD) was performed on Mg_3Sb_2 and $Nb_{0.1}$-Mg_3Sb_2 and the results are shown in **Figure 1**a. The XRD patterns show different preferential orientations relative to the standard intensities, which may influence the transport properties.[14] However, the impact of texture in Mg_3Sb_2 is marginal due to the nearly isotropic interlayer and intralayer bonding network.[15] In comparison with the standard XRD pattern of Mg_3Sb_2, a small impurity peak was found at ~38.4°. Very similar impurity peaks were also observed in $Mg_{3.2-x}Nb_xSb_{1.5}Bi_{0.49}Te_{0.01}$ when $x > 0.5$ and they were assigned to an Nb_3Sb phase.[7a] However, Nb_3Sb is expected to have a diffraction peak with equal intensity at ≈42.1° (Figure 1a), while no such peak is observed in the XRD pattern of $Nb_{0.1}$-Mg_3Sb_2 (Figure 1a) or in the previous work on $Mg_{3.2-x}Nb_xSb_{1.5}Bi_{0.49}Te_{0.01}$.[7a] This peak at ≈38.4° could also be ascribed to Nb metal as it is very near to the intense (110) peak of *bcc* Nb. In order to confirm the nature of the impurity species, ^{93}Nb solid-state nuclear magnetic resonance (NMR) was measured on $Nb_{0.1}$-Mg_3Sb_2 to probe the local atomic and electronic environment of Nb in the sample. The ^{93}Nb NMR spectrum of $Nb_{0.1}$-Mg_3Sb_2 in Figure 1b shows a single resonance near 7190 ppm, which corresponds well to the position and line shape of bulk *bcc* Nb metal. The $Nb_{0.1}$-Mg_3Sb_2 sample and Nb metal also shared a T_1 relaxation time of 5 ms at ambient temperature. Ionized Nb would be expected to have a resonance peak at 0 to –1500 ppm but no signal is observed in that region. ^{93}Nb NMR clearly identifies the presence of metallic Nb in the sample without any evidence for the ionization or incorporation of Nb. As for another bulk, non-destructive technique that is sensitive to local atomic and electronic structure, transmission-mode Nb *K*-edge X-ray absorption spectroscopy (XAS) provides further evidence regarding the oxidation state and local coordination of Nb in the Mg_3Sb_2 sample. The X-ray absorption near-edge structure (XANES) of Nb is very sensitive to oxidation state, shifting by ≈2 eV per formal oxidation state unit from Nb^0 to Nb^{5+}.[16] There is no energy shift between the $Nb_{0.1}$-Mg_3Sb_2 sample and the metallic Nb foil reference, indicating that Nb in the sample is metallic Nb^0 (Figure 1c). The extended X-ray absorption fine structure (EXAFS) of $Nb_{0.1}$-Mg_3Sb_2, which is sensitive to the nearest-neighbor atomic species and interatomic distances, also closely matches that of Nb foil (Figure S1, Supporting Information). The combined results of XRD, NMR, and XAS indicate that Nb presents in its metallic state and is not dissolved in the matrix.
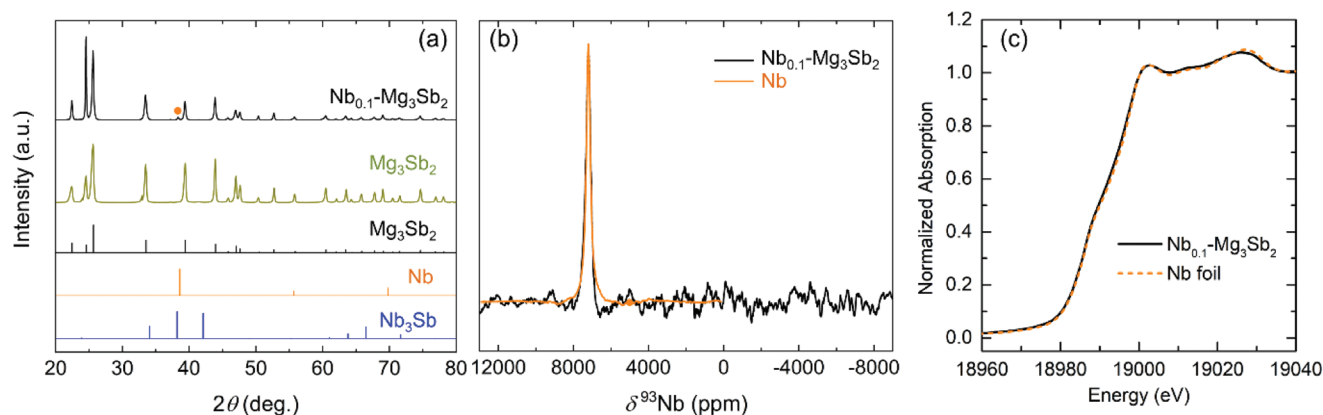

Figure 1. a) XRD pattern of Mg_3Sb_2 and $Nb_{0.1}$-Mg_3Sb_2, compared with standard XRD patterns of Mg_3Sb_2, Nb_3Sb, and Nb. b) ^{93}Nb NMR spectra of $Nb_{0.1}$-Mg_3Sb_2 and Nb metal. The signal intensities are normalized. The spectrum of $Nb_{0.1}$-Mg_3Sb_2 is the variable-offset cumulative spectroscopy (VOCS) summation of five subspectra with equally spaced excitation frequencies. c) Transmission-mode Nb *K*-edge XANES spectra of $Nb_{0.1}$-Mg_3Sb_2 and Nb metal foil.

**ADVANCED
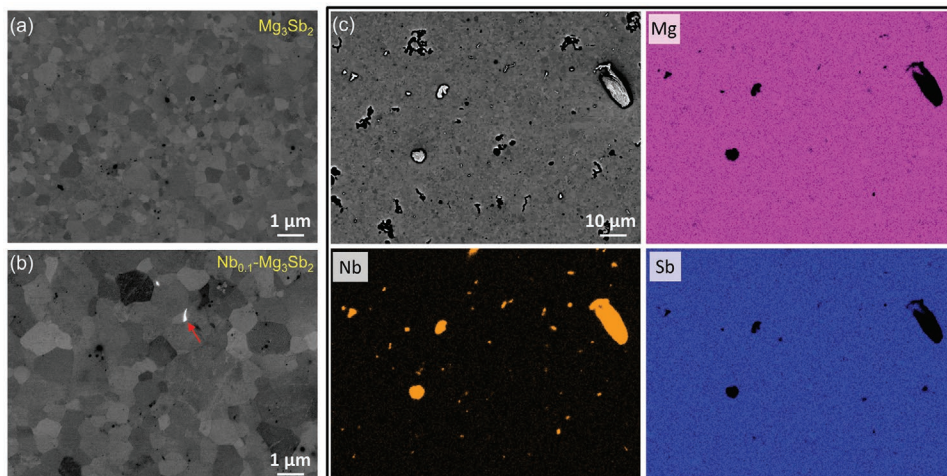SCIENCE NEWS**

www.advancedsciencenews.com

**ADVANCED
FUNCTIONAL
MATERIALS**

www.afm-journal.de

Figure 2. Backscattered electron (BSE) images of a) Mg_3Sb_2, and b) $Nb_{0.1}$-Mg_3Sb_2. The red arrow in (b) denotes an Nb layer present at the GB of Mg_3Sb_2. c) BSE image for a randomly selected large area and the corresponding EDS mapping of $Nb_{0.1}$-Mg_3Sb_2, showing the distribution of Nb, Mg, and Sb. The map of Te is not shown due to its low content which cannot be accurately determined by EDS.

3. Grain Growth of Nb-Added Sample

Figure 2a and 2b show the backscattered electron (BSE) image of a polished surface of pristine Mg_3Sb_2 and $Nb_{0.1}$-Mg_3Sb_2, respectively, which were prepared by ball milling and hot pressing. The mean grain size of both samples was evaluated through the linear intercept method based on the channeling contrast in the BSE images. Details are displayed in Figure S2, Supporting Information. The grain size of Mg_3Sb_2 is ≈0.4 µm (Figure 2a), which is less than half of the grain size of $Nb_{0.1}$-Mg_3Sb_2 (≈1.0 µm) (Figure 2b), even though the same ball-milling and hot-pressing parameters were used to synthesize these two samples. The enlarged grain size upon adding Nb holds for the whole sample as evidenced by a broader view of the BSE images in Figure S3, Supporting Information. This phenomenon was not reported or investigated in previous studies. As the low-temperature carrier mobility of Mg_3Sb_2 is sensitive to the average grain size,[1d,7b,8a,9] this increase in grain size is one factor contributing to improving the electrical conductivity. Further energy-dispersive X-ray spectroscopy (EDS) mapping on a randomly selected surface of $Nb_{0.1}$-Mg_3Sb_2 is shown in Figure 2c. The bright particles in the BSE image are metallic Nb particles. In addition, some Nb is found at GBs in $Nb_{0.1}$-Mg_3Sb_2, as denoted by the red arrow in Figure 2b. Although EDS shows indications of large Nb particles, it does not imply that all the Nb is present in these large metallic lumps. The following APT results will show a thin Nb wetting layer up to tens of nanometers penetrating the grain boundaries of Mg_3Sb_2.

4. Nb Wetting and Interfacial Composition Characterized by APT

We further performed APT to determine the chemical composition and distribution of each constituent element. APT is capable of revealing nano-chemistry in 3D down to the near-atomic scale with a chemical resolution of tens of parts-per-million.[10b,17] **Figure 3**a shows a 52°-tilt scanning electron microscopy (SEM) image of one needle-shaped specimen. Under the Nb particle (Nb source in Figure 3a), a thin wetting layer of Nb is found at the GB of the matrix. The final specimen used for APT characterization is shown in the inset. Figure 3b shows the 3D distribution of Mg, Sb, Nb, and Te. The interface of Mg_3Sb_2/Nb is highlighted by the iso-composition surface of 30 at% Mg. Nb is only found in the wetting layer and not dissolved in the Mg_3Sb_2 matrix. This indicates a negligible solubility of Nb in Mg_3Sb_2 given the high elemental sensitivity of APT.[18] The high density of atoms at the interface is attributed to the local magnification effect during the APT measurement.[17a] A composition profile was computed as a function of the distance to the iso-composition surface delineating regions containing 30 at% Mg or more, and is plotted in Figure 3c. The Nb content in the wetting layer reaches up to 72.9 ± 1.3 at%, and the average content of Sb and Mg are 23.0 ± 2.1 and 3.5 ± 0.7 at%, respectively. The weak signal of Nb in the matrix (Figure 3b,c) is due to the background noise (see detailed explanation in the Supporting Information). The mass spectrum of the Mg_3Sb_2-matrix taken from a region-of-interest away from the GB is shown in Figure S4, Supporting Information. No peaks associated with Nb are present. Sb is found segregated at the Mg_3Sb_2/wetting-layer interface with a peak composition of 59.0 at%. This interface is different from that of Nb-free Mg_3Sb_2 in structure and composition. Our previous work shows a 5% Mg deficiency at GBs in Mg_3Sb_2, forming a potential barrier to hinder charge transport.[10a] The Nb wetting layer could modify the GB resistivity as will be shown by modeling the electrical transport properties. The pure elemental Nb source (Figure S5, Supporting Information) suggests that Sb and Mg are only dissolved in the wetting layer close to the interface and, thus, the stoichiometric composition of the matrix is little influenced. Similar Nb wetting layers present at the GBs of Mg_3Sb_2 are displayed in Figure S6, Supporting Information. The thin Nb wetting layer, found to be tens of nanometers in thickness by APT, is below the detection limits of EDS in the
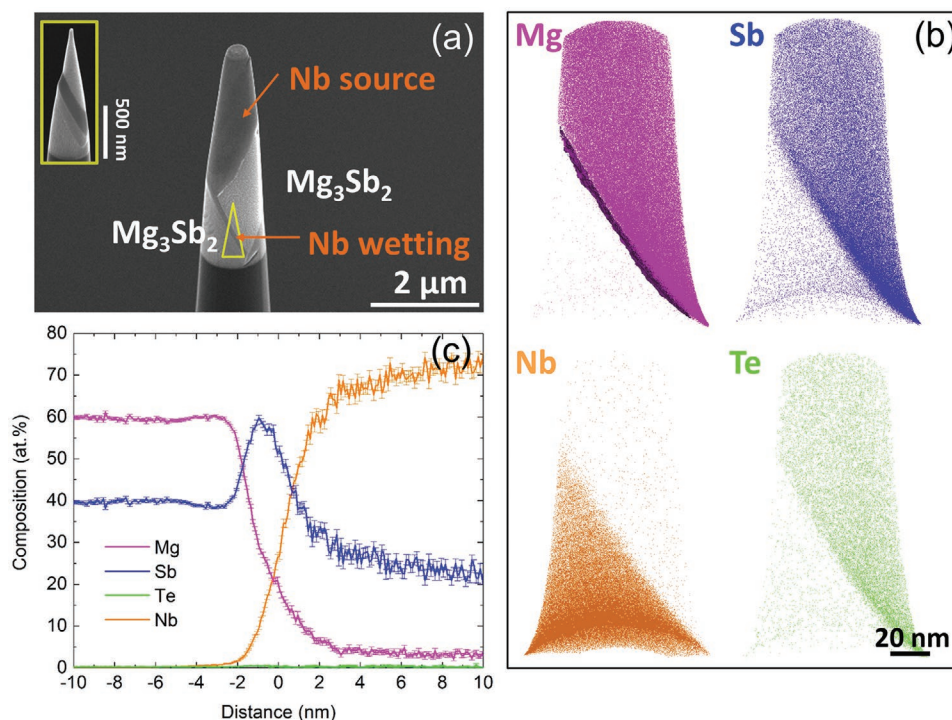
2100258 (3 of 8)

**ADVANCED
SCIENCE NEWS**
www.advancedsciencenews.com

**ADVANCED
FUNCTIONAL
MATERIALS**
www.afm-journal.de

Figure 3. APT characterization of $Nb_{0.1}$-Mg_3Sb_2. a) Scanning electron microscope (SEM) image of a needle-shaped APT specimen, showing the Nb source and wetting layer at the GB of Mg_3Sb_2. The inset displays the final specimen profile; b) 3D elemental distribution of Mg, Sb, Nb, and Te; Note that the density of data points only represents the counts of each element while the composition is determined by the ratio of element counts to the total one; the weak signal of Nb in the matrix is due to background noise as explained in the supplementary information; c) Composition proximity histogram of the iso-composition surface of 30 at% Mg.

SEM and thus not visible in Figure 2. The Nb wetting layer can exist at a large fraction of grain boundaries. This can be ascribed to grain boundary phases or complexion with a given thickness and compositions in thermodynamic equilibrium with the larger Nb, which can almost be seen as reservoirs of Nb.[19]

The above APT results show a negligible solubility of Nb in the Mg_3Sb_2 matrix. Density functional theory calculations also predicted that Nb is not an effective n-type dopant in Mg_3Sb_2 due to the high formation energy of $Nb_{Mg(1)}$ and $Nb_{Mg(2)}$ substitutional defects.[20] Therefore, the addition of Nb in $Nb_{0.1}$-Mg_3Sb_2 cannot change the scattering mechanism of electrons from ionized impurity scattering to a mixed mechanism of ionized impurity scattering and acoustic phonon scattering. Instead, Nb forms a wetting layer between grains and changes the local composition. A change in the interfacial chemistry may modify the interfacial energy and hence the GB migration rate.[21] Provided that the high sintering temperature is kinetically possible to allow for diffusion, the Nb wetting layer offers a possibility for the system to minimize its free energy by balancing the distribution of free energies associated with the matrix phase, metallic Nb particles, and Nb wetting layer at the grain boundaries of the matrix. The wetting layer therefore offers a lever to control the grain size, along with the temperature and duration of the heat treatment, in principle.[22] The details of how a wetting layer modifies the grain growth mechanism will be the topic of very important and interesting future work.

5. Electrical Transport Properties and the Two-Phase Model

In our charge transport measurements (**Figure 4**a,b,c), we find that the electrical conductivity and weighted mobility[23] increase in $Nb_{0.1}$-Mg_3Sb_2 in a wide temperature range from 300 to 600 K. The Nb-free sample shows a temperature dependence of $T^{3.5}$, which is much larger than what would be expected for ionized impurity scattering ($T^{1.5}$). This mechanism hence is not responsible for the low-temperature properties. In contrast, the scattering parameter for GB does not have an exact value but depends on the potential barrier height of the space charge layer.[24] The different scattering parameters mainly originate from different compositions (thus carrier concentration) and grain sizes. By adding Nb, the scattering parameter decreases to 1.6. Based on our chemical and structural characterization, we argue that ionized-impurity scattering cannot underpin this improvement. Rather, it can be attributed to two factors: i) the increase of average grain size in the Nb-added sample, as large-grain semiconductors tend to have higher electrical conductivity due to the reduction of GB density, and ii) the lower GB resistivity due to the additive Nb. As determined by APT, the wetting layer of Nb at GBs alters the GB chemistry (Figure 3c) and hence the local charge transport. The resistivity of a single GB can be estimated simply by a 1D equivalent-circuit model using the following equation:

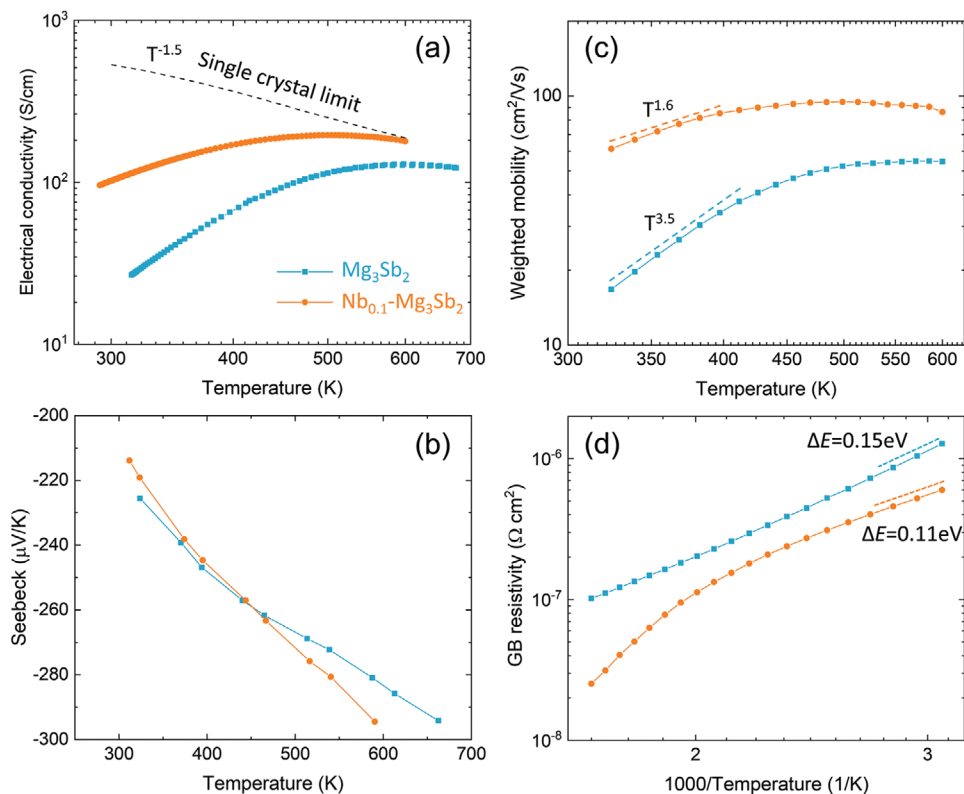$$\sigma_{total}^{-1} \approx \sigma_{bulk}^{-1} + \frac{\tilde{\rho}_{GB}}{d} \tag{1}$$

Figure 4. Charge transport measurement and analyses of n-type Mg_3Sb_2 versus $Nb_{0.1}$-Mg_3Sb_2. a) Experimental electrical conductivity and b) Seebeck coefficient are shown which are used to calculate the c) weighted mobility. The slight difference in the Seebeck coefficient at high temperatures could be due to the modified carrier concentration with temperature. d) Single GB resistivity can be estimated based on the average grain size in Figure 2 (0.4 μm for Mg_3Sb_2 and 1.0 μm for $Nb_{0.1}$-Mg_3Sb_2) and the single-crystal limit (black dash line in (a)). The inverse temperature axis is chosen to calculate the activation energy.

where σ_{total} and σ_{bulk} are the total and bulk electrical conductivity, respectively. $\tilde{\rho}_{GB}$ is the interfacial resistivity of a single GB (in units of Ω cm^2) and d is the average grain size. Based on the BSE images in Figure 2, the average grain sizes of 0.4 and 1.0 μm were taken for Mg_3Sb_2 and $Nb_{0.1}$-Mg_3Sb_2, respectively. The bulk conductivity is estimated using data from a Te-doped Mg_3Sb_2 single crystal from our previous work.[11] In the case where the doping level is significantly different, one can use the weighted mobility or Hall mobility to estimate the bulk conductivity.[23] Temperature-dependent Hall carrier concentration and mobility for Mg_3Sb_2 and $Nb_{0.1}$-Mg_3Sb_2 are shown in Figure S7, Supporting Information. Opposite to the slightly increased carrier concentration by adding Nb in Figure S6b, Supporting Information, Shuai et al.[7a] showed that the carrier concentration decreases with Nb and explained this phenomenon by the weak counter-doping effect of Nb. However, Shuai et al.[7a] not only introduced Nb but also reduced the content of Mg, making a direct comparison difficult. In another work by Shuai et al.,[6] they showed that the carrier concentration slightly decreases with decreasing the content of Mg for n-type Mg_3Sb_2. Thus, the modified carrier concentration could not be attributed to the doping effect of Nb but a reduction in Mg content. The Seebeck coefficient, usually a good measure for the Fermi level, being unchanged after adding Nb demonstrates the nearly same carrier concentration (Figure 4b). Density functional theory calculations also confirmed that Nb is not an efficient dopant for

n-Mg_3Sb_2.[20] Therefore, the slight difference in carrier concentration in this work could not result from Nb doping. Here, we directly use the electrical conductivity of the Te-doped Mg_3Sb_2 single crystal since its carrier concentration and Seebeck coefficients are similar to that of $Nb_{0.1}$-Mg_3Sb_2 in this work. $\tilde{\rho}_{GB}$ was calculated for both of the samples according to Equation 1 and the result is shown in Figure 4d. $\tilde{\rho}_{GB}$ of the Nb-free sample is higher than the Nb-added sample.

In conventional semiconductor studies, the GB resistivity is often associated with a potential barrier through the activation energy ΔE:[24]

$$\tilde{\rho}_{GB} = \tilde{\rho}_0 \exp\left(-\frac{\Delta E}{kT}\right) \qquad (2)$$

where $\tilde{\rho}_0$ is a reference interfacial resistivity. The data in Figure 4b was fitted with Equation 2 and our analysis shows that near room temperature the $Nb_{0.1}$-Mg_3Sb_2 sample has slightly lower activation energy and a two-fold lower $\tilde{\rho}_0$ than that of Mg_3Sb_2. We believe that Nb wetting is responsible for the difference but the mechanism would require further investigation because, in general, both ΔE and $\tilde{\rho}_0$ can depend on the local chemical composition, carrier concentration, dielectric screening, and even temperature.[25]

The thermal conductivity of Mg_3Sb_2 and $Nb_{0.1}$-Mg_3Sb_2 is shown in Figure S8, Supporting Information and compared

with the single-crystal Te-doped Mg_3Sb_2. The impact of Nb on the thermal transport properties is discussed in the supporting information.

6. Conclusions and Outlook

Complementary characterization of Nb-added Mg_3Sb_2 by XRD, NMR, XAS, EDS, and APT demonstrate that Nb remains in a metallic state and does not dissolve into the Mg_3Sb_2 matrix. Adding Nb in Mg_3Sb_2 cannot change the carrier scattering mechanism in the matrix. In contrast, Nb wets the GB to increase the average grain size and decrease the GB resistivity. In combination, these two factors are responsible for the widely observed improved carrier mobility and thermoelectric performance. A similar effect is also expected in other metal-added Mg_3Sb_2-based compounds, such as Co,[12b,13] (Fe, Hf, Ta),[13] and Mn,[1c,12] which show a thermally activated electrical conductivity. The present work indicates that the use of metal Nb additive is an effective GB engineering technique. In the future, examining the distribution of other metal additives in Mg_3Sb_2-based alloys is crucial to understand the underlying scattering mechanism and thus provide promising strategies to improve the thermoelectric performance.

7. Experimental Section

Sample Preparation: Magnesium turnings (99.98%, Alfa Aesar), antimony shot (99.9999%, 5N Plus), tellurium shot (99.999%, 5N Plus), and niobium powder (99.98%, Alfa Aesar) were sealed into stainless-steel jars according to stoichiometric ratios of $Mg_{3.05}Sb_{1.99}Te_{0.01}$ and $Nb_{0.1}Mg_{3.05}Sb_{1.99}Te_{0.01}$ in an argon-filled glove box. The $x = 10\%$ Nb sample was selected for the following reasons. 1) This sample shows slightly higher performance than the $x = 1\%$ sample in Shuai's work.[7a] By examining the $x = 10\%$ Nb sample in our study, we observed a similar effect as in the previous study, even though the carrier concentration is different. 2) No systematic variations in electrical properties were observed in the samples with Nb content from 5% to 15%.[7a] 3) The $x = 10\%$ Nb sample is a representative composition in other works.[14] Thus, we adopted a common composition of Nb to reveal the scattering mechanism of charge carriers at low temperatures. The elements were mechanically alloyed by high-energy ball milling with a high-energy mill (SPEX 8000D) for 2 h. The processed powder was loaded into a graphite die with a half-inch diameter and pressed by an induction-heating rapid hot press for 60 min at 873 K and 45 MPa under argon gas flow. Common experimental methods of ball milling and hot pressing were used to synthesize the samples as the objective of this work is to study the charge carrier scattering mechanism. Therefore, the samples used in this study are representatives of many other thermoelectric alloys and particularly suitable for this fundamental study on Mg_3Sb_2-based materials.

Thermoelectric Property Measurements: Electrical and thermal transport properties were measured from 300 to 600 K for $Nb_{0.1}Mg_{3.05}Sb_{1.99}Te_{0.01}$ and from 300 to 673 K for $Mg_{3.05}Sb_{1.99}Te_{0.01}$ to include the transition temperature from GB-dominated scattering to acoustic phonon-dominated scattering. The electrical resistivity and Hall coefficient measurements were determined using the four-point probe Van der Pauw technique with a 0.8 T magnetic field under a high vacuum with a measurement uncertainty of 10%.[26] The Seebeck coefficients of the samples were obtained using Cr–Nb thermocouples by applying a temperature gradient across the sample to oscillate between ±5 K.[27]

The measurement uncertainty for the Seebeck and electrical conductivity measurements is about 5%. Thermal conductivity was calculated from the relation $\kappa = DdC_p$, where D is the thermal diffusivity measured with a Netzsch LFA 457 laser flash apparatus, d is the geometrical density of the material, and C_p is the heat capacity at constant pressure. The measurement uncertainties for D and d are 3%. C_p of the compounds was estimated by a physics-based model with an uncertainty of about 3%.[28]

X-Ray Diffraction: X-ray diffraction data were collected using a STOE STADI P diffractometer (Cu Kα radiation) in reflection mode (on the hot-pressed samples). XRD data for Nb-free Mg_3Sb_2 were collected with Mo Kα radiation and transformed to angular units for Cu Kα radiation for plotting purposes. The 2θ-ω scan mode (2:1 coupling between 2θ- and ω-position) was chosen, with the ω-position set to $2\theta/2$ for every 2θ position. The scanning range of 2θ was from 10° to 82° with a 0.015° resolution. The scanning step was set to 4° and the scanning period of each step was 720 s (the detector can cover a solid angle of ≈19° with a single step, therefore with a step of 1°, the same 2θ region will be measured 19×).

Solid-State Nuclear Magnetic Resonance Spectroscopy: Static ^{93}Nb spectra were recorded with a simple pulse–acquire (i.e., Bloch decay) sequence at 9.4 T on a Bruker 4.0 mm HX probe with a Bruker Avance III spectrometer. Powder samples were packed into a 4.0 mm diameter zirconia rotor enclosed by a Kel-F polymer cap. A ≈ 20° excitation pulse of 0.5 µs was chosen to account for quadrupolar nutation of ^{93}Nb and to excite a broad frequency range. Relaxation delays of 0.25 s were used to search for ^{93}Nb signals while shorter relaxation delays of 0.05 and 0.02 s were used for the final acquisition of the 8192 × 5 (see below) and 2048 scans of $Nb_{0.1}$-Mg_3Sb_2 and bulk Nb metal, respectively. To overcome the limited excitation frequency range of a single rf pulse, the spectrum of $Nb_{0.1}$-Mg_3Sb_2 was collected with the variable-offset cumulative spectroscopy (VOCS) method.[29] Individual spectra comprising 8192 scans were collected in steps of 240 kHz from 640 kHz (≈6600 ppm) to −320 kHz (≈−3200 ppm). As a check on the validity of this step size, note that the intensity of the peak at ≈7200 ppm was only reduced by 15% at an offset frequency of 300 kHz (compared to 60 kHz offset, chosen to avoid overlapping the resonance position itself). This is consistent with the ≈500 kHz excitation bandwidth expected from the short, high-power pulse. LiNbO$_3$ with an isotropic shift of −1004 ppm was used as a secondary ^{93}Nb shift reference.

X-Ray Absorption Spectroscopy: Nb K-edge XAS was performed at beamline 20-BM at the Advanced Photon Source at Argonne National Laboratory. $Nb_{0.1}$-Mg_3Sb_2 was measured in transmission mode from 18 790 to 20 226 eV while simultaneously measuring an Nb foil reference standard. The beam energy was calibrated with Nb foil by setting the first peak in the derivative spectrum of absorption versus energy to 18 986 eV.[30] The sample was prepared by pressing ≈70 mg of $Nb_{0.1}$-Mg_3Sb_2 into a 7-mm diameter pellet, which gave an edge jump $\Delta\mu\chi$ of ≈0.3 at the Nb K-edge. The sample was loaded into a 3D printed holder and secured with Kapton tape on one side. Four spectra were collected to improve the signal-to-noise ratio; no changes were observed between the spectra, indicating beam stability. Data merging, background subtraction, normalization, and EXAFS data extraction, and Fourier transform were performed in Athena within the Demeter software package.[31] Fourier transform of the k^2-weighted $\chi(k)$ EXAFS data was performed over the k-space range of 3–18 Å^{-1} with a Hanning window function.

Scanning Electron Microscopy: A Zeiss Merlin field-emission SEM was used at 30 kV, 2 pA for the backscattered electron (BSE) imaging, and 15 kV, 6 pA for energy-dispersive X-ray spectroscopy (EDS) mapping. The samples were ground using SiC papers till 4000# and finally polished with a water-free colloidal silica suspension (0.06 µm).

Atom Probe Tomography: The needle-shaped APT specimen was prepared in a dual-beam SEM/FIB system (Helios Nanolab600i, FEI) using the standard "lift-out" method.[32] APT measurements were performed on a LEAP 5000XR (CAMECA) with an ultraviolet (UV) laser (wavelength = 355 nm). The laser pulse energy was 6 pJ, the laser repetition rate was 65 kHz, the specimen base temperature was 40 K,

the detection rate was 0.5 atom per 100 laser pulses on average. The data reconstruction and analyses were processed with the commercial software IVAS 3.8.4 (CAMECA).

Supporting Information

Supporting Information is available from the Wiley Online Library or from the author.

Conflict of Interest

The authors declare no conflict of interest.

Data Availability Statement

Data are available from the author.

[1] a) X. Shi, X. Wang, W. Li, Y. Pei, *Small Methods* **2018**, *2*, 1800022; b) H. Tamaki, H. K. Sato, T. Kanno, *Adv. Mater.* **2016**, *28*, 10182; c) R. Shu, Y. Zhou, Q. Wang, Z. Han, Y. Zhu, Y. Liu, Y. Chen, M. Gu, W. Xu, Y. Wang, W. Zhang, L. Huang, W. Liu, *Adv. Funct. Mater.* **2019**, *29*, 1807235; d) K. Imasato, S. D. Kang, G. J. Snyder, *Energy Environ. Sci.* **2019**, *12*, 965; e) X. Shi, C. Sun, Z. Bu, X. Zhang, Y. Wu, S. Lin, W. Li, A. Faghaninia, A. Jain, Y. Pei, *Adv. Sci.* **2019**, *6*, 1802286; f) J. Mao, H. Zhu, Z. Ding, Z. Liu, G. A. Gamage, G. Chen, Z. Ren, *Science* **2019**, *365*, 495; g) J. Mao, G. Chen, Z. Ren, *Nat. Mater.* **2020**, *20*, 454; h) A. Li, C. Fu, X. Zhao, T. Zhu, *Research* **2020**,

2020, 1934848; i) H. Shang, Z. Liang, C. Xu, J. Mao, H. Gu, F. Ding, Z. Ren, *Research* **2020**, *2020*, 1219461.

[2] a) G. J. Snyder, E. S. Toberer, *Nat. Mater.* **2008**, *7*, 105; b) Y. Yu, D.-S. He, S. Zhang, O. Cojocaru-Mirédin, T. Schwarz, A. Stoffers, X.-Y. Wang, S. Zheng, B. Zhu, C. Scheu, D. Wu, J.-Q. He, M. Wuttig, Z.-Y. Huang, F.-Q. Zu, *Nano Energy* **2017**, *37*, 203.

[3] a) C. L. Condron, S. M. Kauzlarich, F. Gascoin, G. J. Snyder, *J. Solid State Chem.* **2006**, *179*, 2252; b) S. Ohno, K. Imasato, S. Anand, H. Tamaki, S. D. Kang, P. Gorai, H. K. Sato, E. S. Toberer, T. Kanno, G. J. Snyder, *Joule* **2018**, *2*, 141.

[4] J. Zhang, L. Song, S. H. Pedersen, H. Yin, L. T. Hung, B. B. Iversen, *Nat. Commun.* **2017**, *8*, 13901.

[5] a) X. Shi, T. Zhao, X. Zhang, C. Sun, Z. Chen, S. Lin, W. Li, H. Gu, Y. Pei, *Adv. Mater.* **2019**, *31*, 1903387; b) K. Imasato, M. Wood, J. J. Kuo, G. J. Snyder, *J. Mater. Chem. A* **2018**, *6*, 19941.

[6] J. Shuai, B. Ge, J. Mao, S. Song, Y. Wang, Z. Ren, *J. Am. Chem. Soc.* **2018**, *140*, 1910.

[7] a) J. Shuai, J. Mao, S. Song, Q. Zhu, J. Sun, Y. Wang, R. He, J. Zhou, G. Chen, D. J. Singh, Z. Ren, *Energy Environ. Sci.* **2017**, *10*, 799; b) J. J. Kuo, S. D. Kang, K. Imasato, H. Tamaki, S. Ohno, T. Kanno, G. J. Snyder, *Energy Environ. Sci.* **2018**, *11*, 429.

[8] a) M. Wood, J. J. Kuo, K. Imasato, G. J. Snyder, *Adv. Mater.* **2019**, *31*, 1902337; b) Y. Pan, M. Yao, X. Hong, Y. Zhu, F. Fan, K. Imasato, Y. He, C. Hess, J. Fink, J. Yang, B. Büchner, C. Fu, G. J. Snyder, C. Felser, *Energy Environ. Sci.* **2020**, *13*, 1717.

[9] T. Kanno, H. Tamaki, H. K. Sato, S. D. Kang, S. Ohno, K. Imasato, J. J. Kuo, G. J. Snyder, Y. Miyazaki, *Appl. Phys. Lett.* **2018**, *112*, 033903.

[10] a) J. J. Kuo, Y. Yu, S. D. Kang, O. Cojocaru-Miredin, M. Wuttig, G. J. Snyder, *Adv. Mater. Interfaces* **2019**, *6*, 1900429; b) Y. Yu, C. Zhou, S. Zhang, M. Zhu, M. Wuttig, C. Scheu, D. Raabe, G. J. Snyder, B. Gault, O. Cojocaru-Mirédin, *Mater. Today* **2020**, *32*, 260.

[11] K. Imasato, C. Fu, Y. Pan, M. Wood, J. J. Kuo, C. Felser, G. J. Snyder, *Adv. Mater.* **2020**, *32*, 1908218.

[12] a) X. Chen, H. Wu, J. Cui, Y. Xiao, Y. Zhang, J. He, Y. Chen, J. Cao, W. Cai, S. J. Pennycook, Z. Liu, L.-D. Zhao, J. Sui, *Nano Energy* **2018**, *52*, 246; b) F. Zhang, C. Chen, H. Yao, F. Bai, L. Yin, X. Li, S. Li, W. Xue, Y. Wang, F. Cao, X. Liu, J. Sui, Q. Zhang, *Adv. Funct. Mater.* **2020**, *30*, 1906143.

[13] J. Mao, J. Shuai, S. Song, Y. Wu, R. Dally, J. Zhou, Z. Liu, J. Sun, Q. Zhang, C. Dela Cruz, S. Wilson, Y. Pei, D. J. Singh, G. Chen, C. W. Chu, Z. Ren, *Proc. Natl. Acad. Sci. U. S. A.* **2017**, *114*, 10548.

[14] S. Song, J. Mao, J. Shuai, H. Zhu, Z. Ren, U. Saparamadu, Z. Tang, B. Wang, Z. Ren, *Appl. Phys. Lett.* **2018**, *112*, 092103.

[15] J. Zhang, L. Song, M. Sist, K. Tolborg, B. B. Iversen, *Nat. Commun.* **2018**, *9*, 4716.

[16] a) S. A. Howard, C. N. Singh, G. J. Paez, M. J. Wahila, L. W. Wangoh, S. Sallis, K. Tirpak, Y. Liang, D. Prendergast, M. Zuba, J. Rana, A. Weidenbach, T. M. McCrone, W. Yang, T.-L. Lee, F. Rodolakis, W. Doolittle, W.-C. Lee, L. F. J. Piper, *APL Mater.* **2019**, *7*, 071103; b) K. J. Griffith, K. M. Wiaderek, G. Cibin, L. E. Marbella, C. P. Grey, *Nature* **2018**, *559*, 556.

[17] a) B. Gault, M. P. Moody, J. M. Cairney, S. P. Ringer, *Atom Probe Microscopy*, Vol. *160*, Springer Science & Business Media, Berlin **2012**; b) Y. Yu, S. Zhang, A. M. Mio, B. Gault, A. Sheskin, C. Scheu, D. Raabe, F. Zu, M. Wuttig, Y. Amouyal, O. Cojocaru-Miredin, *ACS Appl. Mater. Interfaces* **2018**, *10*, 3609; c) C. Zhou, Y. Yu, Y. L. Lee, B. Ge, W. Lu, O. Cojocaru-Miredin, J. Im, S. P. Cho, M. Wuttig, Z. Shi, I. Chung, *J. Am. Chem. Soc.* **2020**, *142*, 15172.

[18] D. Haley, A. J. London, M. P. Moody, *Microsc. Microanal.* **2020**, *26*, 964.

[19] P. R. Cantwell, T. Frolov, T. J. Rupert, A. R. Krause, C. J. Marvel, G. S. Rohrer, J. M. Rickman, M. P. Harmer, *Annu. Rev. Mater. Res.* **2020**, *50*, 465.

[20] P. Gorai, B. R. Ortiz, E. S. Toberer, V. Stevanović, *J. Mater. Chem. A* **2018**, *6*, 13806.

[21] R. W. Balluffi, J. W. Cahn, *Acta Metall.* **1981**, *29*, 493.

[22] A. R. Kalidindi, C. A. Schuh, *J. Mater. Res.* **2017**, *32*, 1993.

[23] G. J. Snyder, A. H. Snyder, M. Wood, R. Gurunathan, B. H. Snyder, C. Niu, *Adv. Mater.* **2020**, *32*, 2001537.

[24] J. Y. W. Seto, *J. Appl. Phys.* **1975**, *46*, 5247.

[25] A. Y. C. Yu, *Solid-State Electron.* **1970**, *13*, 239.

[26] K. A. Borup, J. de Boor, H. Wang, F. Drymiotis, F. Gascoin, X. Shi, L. Chen, M. I. Fedorov, E. Müller, B. B. Iversen, G. J. Snyder, *Energy Environ. Sci.* **2015**, *8*, 423.

[27] S. Iwanaga, E. S. Toberer, A. LaLonde, G. J. Snyder, *Rev. Sci. Instrum.* **2011**, *82*, 063905.

[28] M. T. Agne, K. Imasato, S. Anand, K. Lee, S. K. Bux, A. Zevalkink, A. J. E. Rettie, D. Y. Chung, M. G. Kanatzidis, G. J. Snyder, *Mater. Today Phys.* **2018**, *6*, 83.

[29] D. Massiot, I. Farnan, N. Gautier, D. Trumeau, A. Trokiner, J. P. Coutures, *Solid State Nucl. Magn. Reson.* **1995**, *4*, 241.

[30] A. Thompson, D. Attwood, E. Gullikson, M. Howells, K.-J. Kim, J. Kirz, J. Kortright, I. Lindau, Y. Liu, P. Pianetta, A. Robinson, J. Scofield, J. Underwood, G. Williams, H. Winick, *X-Ray Data Booklet*, 3rd ed, Lawrence Berkeley National Laboratory, Berkeley CA, USA **2009**.

[31] B. Ravel, M. Newville, *J. Synchrotron. Radiat.* **2005**, *12*, 537.

[32] K. Thompson, D. Lawrence, D. J. Larson, J. D. Olson, T. F. Kelly, B. Gorman, *Ultramicroscopy* **2007**, *107*, 131.